

Collective variable model for the dynamics of liquid crystal skyrmions

Tomás Alvim ^{1,2}, Margarida M. Telo da Gama ^{1,2} & Mykola Tasinkevych ^{1,2,3,4}✉

Liquid crystal skyrmions are topologically protected spatially-localized distortions of the director field which exhibit particle-like properties including translational motion in oscillating electric fields. Here, we develop a collective variable model of the skyrmion dynamics, extending the approach of Long and Selinger proposed earlier for one dimensional systems. The model relates the skyrmion motion to a complex dynamics of the width of the twist wall around the skyrmion core. The width evolves in a non-reciprocal way, quantifying squirming deformations of the high twist region within on and off states of the field. We analyze in details the average skyrmion velocity as a function of the frequency and strength of the field as well as its duty cycle. The model predictions agrees qualitatively with experiments and results of numerical minimization of the Frank-Oseen model. Our results provide insights into the conditions necessary to observe velocity reversal as a function of the field parameters.

¹Centro de Física Teórica e Computacional, Faculdade de Ciências, Universidade de Lisboa, 1749-016 Lisboa, Portugal. ²Departamento de Física, Faculdade de Ciências, Universidade de Lisboa, 1749-016 Lisboa, Portugal. ³SOFT Group, School of Science and Technology, Nottingham Trent University, Clifton Lane, Nottingham NG11 8NS, UK. ⁴International Institute for Sustainability with Knotted Chiral Meta Matter, Hiroshima University, Higashihiroshima 739-8511, Japan. ✉email: mykola.tasinkevych@ntu.ac.uk

Topological solitons emerge in nonlinear field theories as spatially localized and topology-stabilized configurations¹. Examples include kink or antikink solutions of the ϕ^4 model², Skyrme solitons (skyrmions) in nuclear physics³, vortex-like spin configurations known as magnetic skyrmions in condensed matter systems^{4–9}, as well as torons, hopfions, and baby skyrmions in confined chiral liquid crystals (LCs)^{10–22}. From the fundamental science point of view, solitons exhibit particle-like behavior and have been proposed as a model of the nucleon³. From a practical standpoint, magnetic skyrmions can be moved by using weak electric currents²³, which opens an avenue to exploit magnetic skyrmions in spintronic applications, e.g., in racetrack memory devices²⁴.

LC skyrmions can also be brought into controlled directional motion in oscillating electric fields^{12,13}. Numerical minimization of the Frank-Oseen elastic free energy¹² has uncovered the basic physical mechanism of skyrmion translation, which is related to the non-reciprocal relaxation dynamics of the chiral director field in time-modulated electric fields. More specifically, the boundary of a region with the high director twist undergoes deformations that resemble squirming surface waves of biological microorganisms undergoing self-propulsion. Contrary to microswimmers, however, the squirming motion of skyrmions is not related/accompanied to/by LC material flows and is purely due to the reorientation dynamics of the director field. In the present work, we provide a quantitative measure of these squirming undulations of the high twist regions, in terms of the thickness of the twist wall around the skyrmion core.

Experimental results have shown that the skyrmion velocity sensitively depends on the frequency, strength, and duty cycle of the pulse width modulated driving electric field. In multi-skyrmion systems, unexpected collective behavior has been reported experimentally including light-controlled skyrmion interactions and self-assembly¹⁴, reconfigurable cluster formation, and formation of large-scale skyrmion crystals mediated by out-of-equilibrium elastic interactions¹⁵. Driven LC skyrmions offer a distinct paradigm of solitonic active particle-like structures without mass transport^{12,13}. The experimental setups employed to stabilize and study active skyrmions are similar to those used in LC display technologies²⁵. As such, the controlled motion of a large number of skyrmions holds potential for the development of reconfigurable electro-optic materials²⁶. Numerical analysis based on minimization of the Frank-Oseen^{12,13} and Landau-de Gennes^{18–20} free energies have successfully reproduced many experimental results regarding the structure and dynamics of LC skyrmions. These fine-grained approaches fully resolve the spatio-temporal structure of the LC order parameter field and are computationally costly, which does not allow a comprehensive sampling of the whole space of the model parameters.

To overcome this challenge, Long and Selinger proposed a coarse-grained model of the skyrmion dynamics²², where a few collective variables approximately describe the skyrmion configuration and its response to an external field. The method was applied to characterize the motion of one-dimensional sine-Gordon solitons, and its extension to two-dimensional (2D) skyrmions was outlined without detailed analysis. The method of Long and Selinger is similar to the one used in nonlinear field theories to construct a reduced description of soliton interactions in terms of several relevant collective variables^{2,27}. This method is also similar to that employed in refs. ^{28–30} to study the dynamics of magnetic skyrmions, with the only difference that in those studies the skyrmion position was the only collective variable, i.e., it was assumed that the magnetic structure translates at a given speed as a rigid body³¹. By contrast,²² introduced an internal degree of freedom – the width of the twisted wall that changes as the skyrmion moves.

Here, based on the original idea of ref. ²² we present a collective variable model of driven motion of LC skyrmions in 2D. We stress that in this study only full skyrmions are considered. The developed minimal model demonstrates that the net displacement of the skyrmion under periodic switching of the electric field on and off is related to the complex dynamics of the width of the twist wall around the skyrmion. The width provides a quantitative characteristic of the high twist region and changes in a non-reciprocal way within each on and off state of the field, resulting in the net skyrmion displacement over one period of the electric field. We find that the skyrmion velocity is proportional to the time derivative of the polar angle specifying the far-field director, which responds to the changes in the applied voltage, and the speed is maximal just after the electric field has been turned on or off. The analysis also demonstrates that velocity reversal with changing the field frequency or the duty cycle is related to the ratio of the director relaxation times during the field-on and field-off states. The relaxation time is given by the inverse square of the external effective field, which also includes a fictitious component mimicking the effects of homeotropic boundary conditions in real 3D systems. We emphasize, that the approach developed here can straightforwardly be applied to magnetic skyrmions. One just needs to use a suitable Ansatz for the magnetization field into the Landau-Lifshitz-Gilbert equation³² in order to derive the equations governing the evolution of the corresponding internal degrees of freedom (Ansatz parameters) of the magnetic skyrmion.

Results

Skyrmion Ansatz. We assume that at zero electric field, the far-field nematic director is aligned along the z -axis, and define an axisymmetric Ansatz for the skyrmion configuration with the winding number equal unity as follows:

$$\begin{aligned} n_x^a(\mathbf{r}; \xi) &= \sin(\Xi(r; \xi)) \cos(\Psi(\mathbf{r})) \\ n_y^a(\mathbf{r}; \xi) &= \sin(\Xi(r; \xi)) \sin(\Psi(\mathbf{r})) \\ n_z^a(\mathbf{r}; \xi) &= \cos(\Xi(r; \xi)), \end{aligned} \quad (1)$$

where

$$\Xi(r; \xi) = \pi + \pi H\left(r - \frac{p}{2}\right) \left[\exp\left(-\frac{(r - \frac{p}{2})^2}{\xi^2}\right) - 1 \right] \quad (2)$$

$$\Psi(\mathbf{r}) = \arctan\left(\frac{x - x_s}{y - y_s}\right) + \frac{\pi}{2} \quad (3)$$

$$r = \sqrt{(x - x_s)^2 + (y - y_s)^2}. \quad (4)$$

Here H is the Heaviside step function, p is the cholesteric pitch and r is the distance from a point $(x, y)^T$ to the skyrmion center at $(x_s, y_s)^T$, where the superscript T denotes the transposition operation. The parameter ξ controls the width of the twisted wall which separates the skyrmion core of size $p/2$ with the vectorized director pointing in $-\hat{z}$ direction from the far-field director aligned along \hat{z} . The function $\Xi(r; \xi)$ is plotted in Fig. 1, and from this point onwards, lengths are given in units of the cholesteric pitch p .

In this study, we consider LCs with positive dielectric anisotropy $\Delta\epsilon$, and thus when an external electric field is applied perpendicular to \hat{z} , the skyrmion will morph to a non-symmetric so-called bimeron³³ configuration, with the far-field director $\mathbf{n}_0 = (\sin \Theta \cos \Phi, \sin \Theta \sin \Phi, \cos \Theta)^T$ tilted away from \hat{z} . For strong enough electric fields, \mathbf{n}_0 will be in the (x, y) plane. The resulting bimeron configuration has no analytical representation, therefore we resort to a simple approximation, which relies on a

uniform local rotation of the symmetric director field in Eq. (1)

$$\mathbf{n}(\mathbf{r}; \Theta, \Phi, \xi) = \mathbf{R}(\Theta, \Phi) \mathbf{n}^a(\mathbf{r}; \xi). \quad (5)$$

Here, $\mathbf{R}(\Theta, \Phi)$ is the rotation matrix which transforms \hat{z} to \mathbf{n}_0 . Figure 2a illustrates the director configuration of the original Ansatz in Eq. (1), and Fig. 2b, c shows the approximation (5) of the bimeron configurations for $\Theta = \pi/4$ and $\pi/2$.

One way to obtain \mathbf{n}_0 is to rotate \hat{z} by Θ about the axis $(-\sin \Phi, \cos \Phi, 0)$ in the (x, y) plane. The parameterization of the rotation matrix \mathbf{R} , in terms of the axis and the angle, is given by Rodrigues formula³⁴

$$\mathbf{R}(\Theta, \Phi) = \mathbf{I} + \sin \Theta \mathbf{M}(\Phi) + (1 - \cos \Theta) \mathbf{M}^2(\Phi), \quad (6)$$

where \mathbf{I} is the identity matrix and

$$\mathbf{M}(\Phi) = \begin{bmatrix} 0 & 0 & \cos \Phi \\ 0 & 0 & \sin \Phi \\ -\cos \Phi & -\sin \Phi & 0 \end{bmatrix}. \quad (7)$$

The rotated configuration (5) depends on the five parameters $\xi, x_s, y_s, \Theta, \Phi$, and in the next section we construct equations describing their time evolution in response to switching the external electric field on and off.

Frank-Oseen free energy and a dissipation rate. We adopt the one elastic constant $K_{11} = K_{22} = K_{33} = K$ approximation, and present below all the equations in a dimensionless form, with Kp set as the unit of energy and $\gamma p^2 K^{-1}$ the unit of time, where γ is the rotational viscosity. For the unit of the electric field we use $\sqrt{2K/\epsilon_0 \Delta \epsilon p^2}$, where ϵ_0 is the vacuum permittivity and $\Delta \epsilon$ is the dielectric anisotropy. We consider here a two-dimensional system

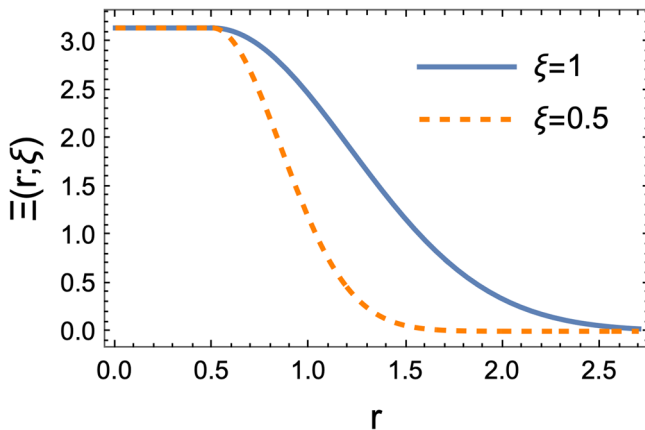


Fig. 1 Polar angle of the director Ansatz for a skyrmion. $\Xi(r; \xi)$ defined in Eq. (2) as a function of the distance r from the skyrmion center, for two values of the wall thickness $\xi = 1$ and 0.5 . With increasing r the director field rotates by π , which corresponds to a full-skyrmion.

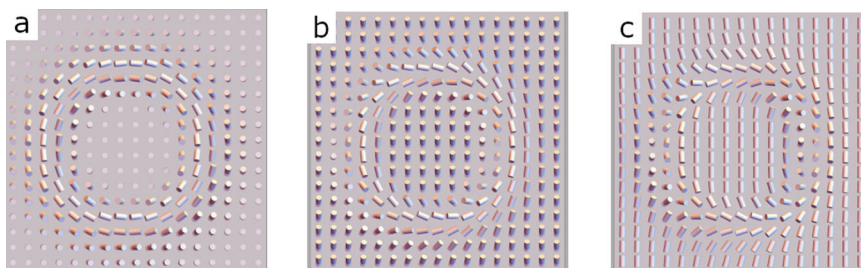


Fig. 2 Director profile of the skyrmion Ansatz. The director field of the skyrmion configurations for $\Theta = 0, \pi/4, \pi/2$, **a**, **b**, and **c**, respectively; $\Phi = -\pi/2$ in all the cases. The director field is represented by cylinders. The skyrmion core has the same alignment as the background. The wall thickness parameter is $\xi = 0.7$.

where the director field varies in the (x, y) plane. At zero field this corresponds to a three-dimensional system that is translationally invariant along the skyrmion's symmetry axis, see Fig. 2a. This analogy, however, does not apply to deformed configurations, as shown in Fig. 2b, c, obtained at non-zero fields. The dimensionless Frank-Oseen elastic free energy per length along z -axis reads:

$$F = \int \left((\nabla \cdot \mathbf{n})^2 + (\nabla \times \mathbf{n})^2 + 2\pi \mathbf{n} \cdot \nabla \times \mathbf{n} - \frac{(\mathbf{E} \cdot \mathbf{n})^2}{2} \right) d^2 r. \quad (8)$$

The integral is over the whole plane (x, y) , and the effective electric field $\mathbf{E} = (0, -E, W)^T$, where E is the amplitude of the real electric field applied in the $-\hat{y}$ direction, and W accounts for effects of the homeotropic anchoring conditions at the cell surfaces of a three-dimensional system. This is a standard approach to account for boundary-induced anisotropy through an effective bulk electric field in 2D system, see ref. 18, for a detailed discussion. We introduce the ratio m of the electric and elastic energy in the following way

$$m^2 = (E^2 + W^2). \quad (9)$$

As we show below, m controls the relaxation time of the director when the electric field is turned on and off.

The Rayleigh dissipation function per unit length, due to the director reorientation, has the form²²:

$$D = \frac{1}{2} \int \left\| \frac{d\mathbf{n}}{dt} \right\|^2 d^2 r = \frac{1}{2} \int \left\| \frac{\partial \mathbf{n}}{\partial \Theta} \dot{\Theta} + \frac{\partial \mathbf{n}}{\partial \Phi} \dot{\Phi} + \frac{\partial \mathbf{n}}{\partial \mathbf{r}_s} \cdot \dot{\mathbf{r}}_s + \frac{\partial \mathbf{n}}{\partial \xi} \dot{\xi} \right\|^2 d^2 r. \quad (10)$$

Here the double vertical lines mean the absolute value of the enclosed vector. The dynamic equations for the skyrmion collective variables are obtained from the force balance²²

$$\frac{\partial D}{\partial \dot{\Theta}} + \frac{\partial F}{\partial \Theta} = 0, \quad (11)$$

$$\frac{\partial D}{\partial \dot{\Phi}} + \frac{\partial F}{\partial \Phi} = 0, \quad (12)$$

$$\frac{\partial D}{\partial \dot{\xi}} + \frac{\partial F}{\partial \xi} = 0, \quad (13)$$

$$\frac{\partial D}{\partial \dot{x}_s} = 0, \quad (14)$$

$$\frac{\partial D}{\partial \dot{y}_s} = 0, \quad (15)$$

where dots above the parameters indicate time derivatives, and the two last equations take into account that the free energy F does not depend on the skyrmion position $(x_s, y_s)^T$. We fix the reference frame such that \mathbf{E} changes in the (y, z) plane only, which will lead to the skyrmion motion along the x -axis. Any

initial background director will, after a short transient, reorient and remain in the (y, z) plane, i.e., Φ will approach a constant equal $\pi/2$ or $-\pi/2$ depending on the initial orientation. Here we set up the system such that this value is always $-\pi/2$. As we show below the skyrmion displacement proceeds in the direction perpendicular to the plane in which the background director varies, in agreement with previous experimental¹² and theoretical results²². Considering the above, in the following we consider only Eqs. (11), (13) and (14). This system of equations is not amenable to analytical solutions, and thus we developed a hybrid analytico-numerical method to analyze them. The general algebraic structure of the terms in the dissipation rate D and the free energy F may be written as a product of two tensors

$$\mathbf{B}_{ij}(\Theta) \int \mathbf{T}_{ij}(\xi, \mathbf{r}) d^2r, \quad (16)$$

where the summation over repeated indices is implied. Tensors \mathbf{B}_{ij} depend on the far-field background parameter. They are expressed as products $\mathbf{R}_{ki}\mathbf{R}_{kj}$ or $\mathbf{R}_{ki}\partial\mathbf{R}_{kj}/\partial\Theta$ and can be calculated analytically. The spatially varying tensors $\mathbf{T}_{ij}(\xi, \mathbf{r})$ depend only on the thickness ξ of the twisted wall and have the form of products of pairs selected from the components of \mathbf{n}^a in (1), spatial derivatives of \mathbf{n}^a or its derivatives with respect to x_s and ξ . The double integrals in Eq. (16) are calculated numerically and the resulting functions of ξ are fitted to simple expressions as detailed in Methods below.

We assume that the dynamics of Θ is not dependent on the presence of the skyrmion, and evaluate the lhs and the rhs in Eqs. (11) inserting the uniform far-field \mathbf{n}_0 into Eqs. (8) and (10). With this, we obtained the following system of dynamical equations:

$$\dot{\Theta} = (E \sin \Theta + W \cos \Theta)(E \cos \Theta - W \sin \Theta), \quad (17)$$

$$\dot{\xi} = -d_1(\xi) \left(-\frac{15.5}{\xi^2} + d_2(\xi)(1 + \cos \Theta) + d_3(\xi)[W^2 - E^2 + 3 \cos(2\Theta)(E^2 + W^2) + 6EW \sin(2\Theta)] \right), \quad (18)$$

$$\dot{x}_s = d_4(\xi)\dot{\Theta}. \quad (19)$$

The explicit expressions for $d_1(\xi)$ up to $d_4(\xi)$ and the numerical procedure for how they have been obtained are provided in the ‘‘Methods’’ section below. Equation (17) for the background angle $\Theta(t)$ admits an analytical solution which we present in Methods as well.

Linear stability analysis. In this section, we carry out a linear stability analysis of the system of Eqs. (17)–(19) around their fixed points. The skyrmion will evolve towards stable fixed points and also spend time near them in the case of time-dependent electric fields. The behavior resulting from the linearized equations sheds light on the evolution of the full nonlinear system. Since the dynamics of x_s is slaved to that of ξ and Θ , Eq. (19), it is sufficient to consider only Eqs. (17) and (18).

Setting the rhs of Eq. (17) to zero renders two fixed point solutions for the polar angle $\Theta^* = \arctan(E/W)$ and $\Theta^* = -\arctan(W/E)$. It turns out that the second solution corresponds to an unstable fixed point. The fixed point for the twist wall thickness ξ^* follows from setting $\Theta = \Theta^*$ on the rhs of Eq. (18) and finding the roots of the resulting equation numerically. The resulting fixed point solution ξ^* is plotted in Fig. 3 as a function of m , and is well approximated by m^{-2} in agreement with¹⁸. In experiments as well as numerical simulations, the skyrmion is only stable in a finite range of electric fields^{18,35}.

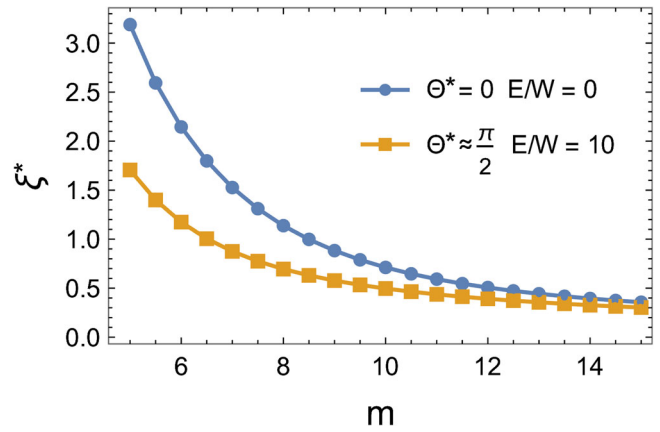


Fig. 3 Equilibrium thickness of the skyrmion twist wall. The stable wall thickness ξ^* as a function of $m = \sqrt{E^2 + W^2}$, at two values of the equilibrium Θ^* . The lines are to guide the eyes.

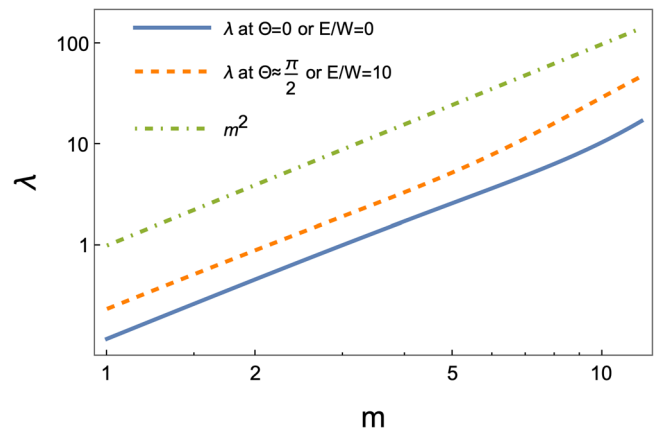


Fig. 4 Inverse relaxation time of the twist wall thickness. λ , which is the derivative of the rhs of equation (18) with respect to ξ evaluated at ξ^* , as a function of $m = \sqrt{E^2 + W^2}$, for two equilibrium values of $\Theta = 0$ and $\pi/2$. For comparison the curve $\propto m^2$ is also shown.

We linearize equations (17) and (18) near the fixed point (Θ^*, ξ^*)

$$\dot{\Theta} \approx -(E^2 + W^2)(\Theta - \Theta^*), \quad (20)$$

$$\dot{\xi} \approx -[\xi - \xi^*]\lambda(m, E/W), \quad (21)$$

where $\lambda(m, E/W)$ is the derivative of the rhs of Eq. (18) with respect to ξ evaluated at ξ^* . λ as a function of m is shown in Fig. 4, and it is approximately $\propto m^2$ in the relevant range of m . We emphasize, that the relaxation of ξ upon turning the field off is slower as compared to the field-driven response, which provides additional means to control the skyrmion dynamics.

Next, we substitute the solutions $\Theta(t)$ and $\xi(t)$ of the linearized equations (20) and (21) into (19), which renders

$$\dot{x}_s(t) = -m^2 e^{-m^2 t} (\Theta_0 - \Theta^*) (\xi^* + (\xi_0 - \xi^*) e^{-\lambda t}), \quad (22)$$

where we replaced $d_4(\xi)$ with ξ for simplicity (see Methods where $d_4(\xi)$ is defined), and Θ_0 is the initial value of the far-field polar angle. An approximate equation (22) describes the skyrmion velocity in the vicinity of the fixed point (Θ^*, ξ^*) , therefore the initial values Θ_0 and ξ_0 must be taken close to the fixed point.

We find that in the relevant range of $m \lambda > 0$, as shown in Fig. 4, and thus the late-time behavior of the velocity in (22) is governed by the term $\propto \exp(-m^2 t)$, and the term $\propto \exp(-\lambda t)$ may be neglected. With this in mind, the approximate solution

$x_s(t)$ of (22) may be written in the following form

$$x_s(t) = \exp(-m^2 t)(\Theta_0 - \Theta^*)\xi^* + x_s(\infty), \quad (23)$$

$$\Delta x_s \equiv x_s(\infty) - x_s(0) = \xi^*(\Theta^* - \Theta_0), \quad (24)$$

where we have also defined the net skyrmion displacement Δx_s . Equation (24) highlights two important features in determining the net skyrmion displacement: i) a rotation from the vertical configuration $\Theta_0 = 0$ to a larger Θ^* , e.g. when the electric field E is applied, yields a positive displacement increasing with $\Delta\Theta \equiv \Theta^* - \Theta_0$; ii) the displacement depends on the stable wall thickness ξ^* . Figure 3 shows that ξ^* decreases with increasing both m and E/W .

Imagine that the electric field E undergoes step-like oscillations between zero and a sufficiently high value, such that $\Theta^*(E) \approx \pi/2$. Additionally, assume that the oscillation period is large enough such that Θ oscillates between the two equilibrium values 0 and $\pi/2$. Then, during the field on state, the net skyrmion displacement $\Delta x_s[\text{off} \rightarrow \text{on}] \approx \pi\xi^*(m_{\text{on}}, E)/2$, while the net skyrmion displacement during the off state is $\Delta x_s[\text{on} \rightarrow \text{off}] \approx -\pi\xi^*(m_{\text{off}}, 0)/2$. The expressions in the square brackets indicate the situations when the electric field has changed from 0 to E , [off \rightarrow on], or from E to 0, [on \rightarrow off], also $m_{\text{off}} = W < m_{\text{on}} = \sqrt{W^2 + E^2}$. Based on the numerical results displayed in Fig. 3, we conclude that $\xi^*(m_{\text{off}}, 0) > \xi^*(m_{\text{on}}, E)$ and the net skyrmion's displacement over one period of the electric field is $\Delta x_s[\text{off} \rightarrow \text{on}] + \Delta x_s[\text{on} \rightarrow \text{off}] < 0$: the skyrmion translates in the $-\hat{x}$ direction.

We will show in the next section that in the framework of the full nonlinear model given by Eqs. (17)–(19). The skyrmion velocity can reverse its direction. The numerical solution of the full nonlinear dynamics demonstrates that most of the displacement occurs at early times away from the stable value of ξ , where the linear model is not valid.

Skyrmion relaxation upon abrupt changes in the electric field.

Equation (17) can be solved analytically, where the corresponding solution $\Theta(t)$ is given in Methods, Eq. (32), and Eqs. (18), (19) are solved numerically using Mathematica. We first solve for the twist wall thickness $\xi(t)$, which is coupled to $\Theta(t)$, and then determine the skyrmion position $x_s(t)$. Figure 5 depicts the time

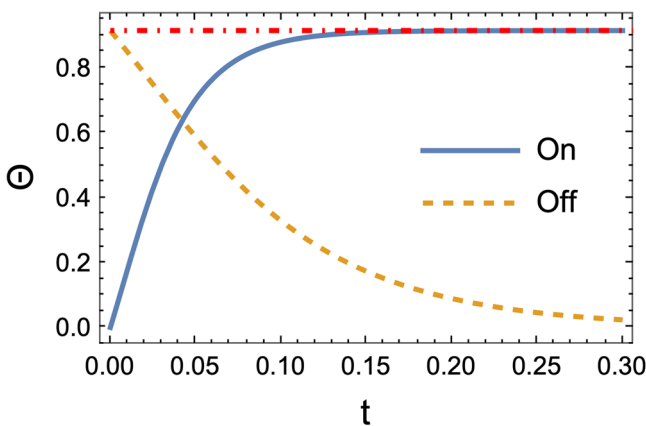


Fig. 5 Relaxation dynamics of the polar angle of the far-field director. Θ as a function of time when the electric field changes abruptly from 0 to E , blue curve. After the angle completely relaxes towards the horizontal dashed-dotted red line, the field is turned off and the corresponding $\Theta(t)$ is shown by the dashed orange curve, where $t = 0$ coincides with the time of turning the field off. The magnitude of the electric field is 30% larger than that of the anchoring, $E/W = 1.3$ and $m_{\text{on}} = \sqrt{E^2 + W^2} = 6$. The horizontal dashed red line corresponds to $\arctan(1.3)$. Time is in units of $\gamma p^2 K^{-1}$.

evolution of Θ when the electric field changes abruptly from 0 to some value E (full blue curve), and then after Θ reaches the equilibrium value $\arctan(E/W)$, the field is turned off abruptly and Θ evolves to 0 (dashed orange curve). The solutions converge quickly to those of the linearized Eq. (20), i.e., $\propto \exp(-m^2 t)$. If ξ were constant, the skyrmion displacement would look exactly like $\Theta(t)$, see Eq. (19).

The internal degree of freedom of the skyrmion, the twist wall thickness ξ is shown in Fig. 6. The non-monotonic behavior of $\xi(t)$ at early times, when the field is on, traces back to a specific value of the initial condition $\xi(t=0) > \xi(t=\infty) \equiv \xi^*$. According to the results in Fig. 3, ξ^* decreases with the increasing E , therefore more pronounced non-monotonic behavior of $\xi(t)$ is expected when the field changes from zero to larger values. Thus, the skyrmion speed which is $\propto \xi(t)$ (see Eq. (19)) is largest just after the field is turned on.

Having determined $\xi(t)$ and $\Theta(t)$ enables calculating the skyrmion trajectory

$$x_s(t) \propto \int_0^t \xi(t')\dot{\Theta}(t')dt', \quad (25)$$

where the proportionally constant is the coefficient 0.6 in the function $d_4(\xi)$, Eq. (31).

We evaluate the integral in Eq. (25), starting with the axisymmetric skyrmion configuration, Eq. (1). At $t = 0$ the electric field is set to a value E , and the skyrmion morphs (see Fig. 7b) towards the second fixed point, shown in Fig. 7c. Then, after equilibrium is reached, the field is turned off and the skyrmion relaxes back (see Fig. 7d, e) to the axisymmetric form. The skyrmion trajectory $x_s(t)$ corresponding to this protocol is shown in Fig. 7a together with several representative skyrmion configurations.

When the field is turned on, the far-field director \mathbf{n}_0 tilts away from \hat{z} , dragging the skyrmion along x . When the background reaches $\Theta^* = \arctan(E/W)$ the skyrmion stops, with the corresponding configuration shown in Fig. 7c. Next the field is turned off and \mathbf{n}_0 rotates back to \hat{z} , Fig. 7e. During this field-off state, the relaxation time of Θ is $(E^2 + W^2)/W^2 = 2.7$ times slower

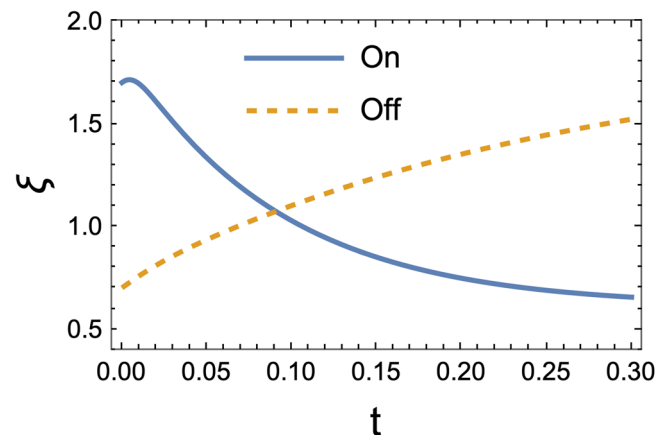


Fig. 6 Relaxation dynamics of the thickness of the skyrmion twist wall.

The thickness ξ of the twist wall around the skyrmion core as a function of time, is calculated numerically by using Eqs. (18) and (17). The blue curve corresponds to the case when the field is changed abruptly from 0 to E . When ξ reaches the equilibrium ξ^* the field is turned off and the corresponding $\xi(t)$ is shown by the dashed orange curve, where $t = 0$ coincides with the time of turning the field off. The subsequent dynamics are represented by the orange curve. $m_{\text{on}} = 10$, $E/W = 1.2$ and time is in units of $\gamma p^2 K^{-1}$.

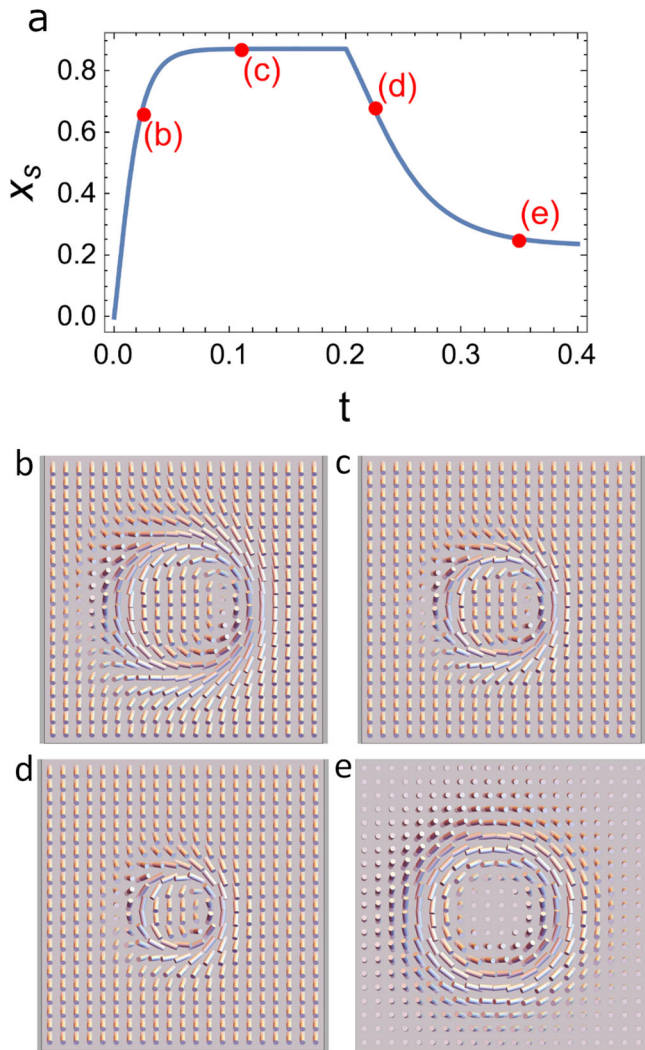


Fig. 7 Skyrmion evolution upon turning the field on and off. **a** Skyrmion position x_s as a function of time t when the electric field is turned on at $t = 0$ and then turned off at $t = 0.2$. In the on state $m_{on} = \sqrt{E^2 + W^2} = 6$ and $E/W = 1.3$. When the field is turned off the background and the position take longer to relax because $m_{off} = W < m_{on}$. Time is in units of $\gamma p^2 K^{-1}$. **b-e** show director configurations represented by the cylindrical rods. The configurations correspond to the times indicated by **b-e** in panel **a**. **b** the skyrmion moves forward and the twist wall thickness decreases; **c** the stable angle $\Theta = \arctan(1.3)$ was reached, the shrinking continues without skyrmion movement. **d** after the field changes the wall width is at its shortest and the skyrmion moves backwards, **e** the far-field polar angle $\Theta \ll 1$, and the skyrmion speed approaches zero.

than in the preceding field-on state, recall that linear model predicts $\Theta \propto \exp(-m^2 t)$, see Eq. (20).

Equation (24) is valid in the linear regime and predicts a negative displacement under such protocol, because the stable thickness is larger for the off state. However, the opposite is observed here. This can be understood by analyzing Eq. (25). Indeed, the rate of change of Θ is maximal right after the field changes, and is significantly reduced by approaching to the equilibrium where the linear regime holds. Therefore, the initial nonlinear transient of Θ is more relevant in determining the net displacement than the stable thickness ξ^* controlling the skyrmion displacement at late times. This transient is affected by the initial conditions and field parameters, which will be discussed in the following section.

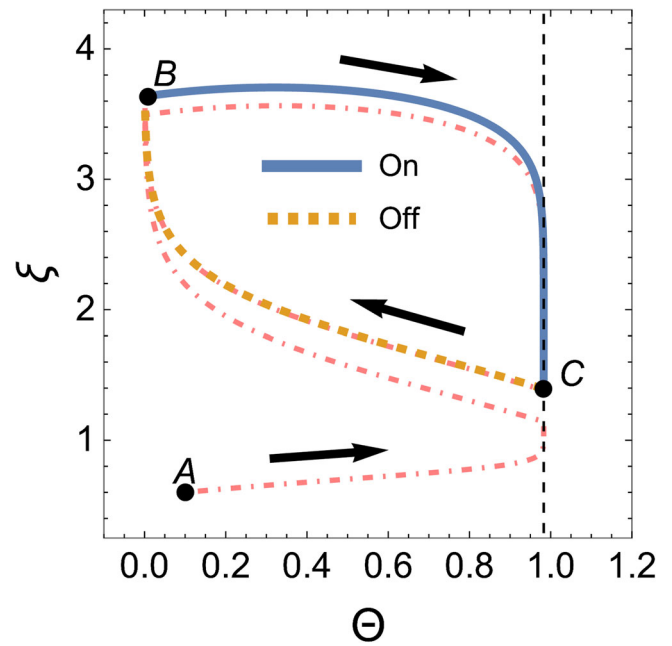


Fig. 8 Steady-state cycle upon periodic turning of the field on and off. Skyrmion trajectory in the (Θ, ξ) phase plane upon periodic switching of the field on and off. The initial configuration corresponds to point A. At the initial time, the field is on, and the corresponding stable polar angle Θ^* is indicated by the dash-dotted magenta curve, while the full blue (field-on state) and the dashed orange (field-off state) curves correspond to the long-time steady-state cycle. The black arrows indicate the direction of the motion. The field is turned on at point B and off at point C. The net skyrmion displacement is proportional to the area enclosed by the loop. The area between the field-on (the full blue curve) trajectory and the horizontal axis is larger than the area between the field-off (the dashed orange curve) trajectory and the horizontal axis, which results in the skyrmion motion in the $+\hat{x}$ direction. The field parameters are $m_{on} = 7, E/W = 1.5, T = 1$ and $\mathcal{D} = 0.5$.

Steady-state cycle in pulse width modulated electric fields: driving protocol 1). We discuss the skyrmion dynamics in a pulse width modulated electric field, which is switched on for a fraction of the period, referred to as the duty cycle \mathcal{D} , and then turned off. The period T is the sum of the field off and on times.

We first consider a driving protocol where the electric field has only one component in the $-\hat{y}$ direction: protocol 1). In the course of time the skyrmion trajectory will approach a characteristic closed loop when plotted in the phase plane (Θ, ξ) , with one example shown in Fig. 8. The loop corresponds to a steady-state cycle and as long as the field continues to oscillate the system follows the loop.

The repeating cycles yield skyrmion motion with a steady average velocity $\langle v \rangle = \Delta x_s / T$, where Δx_s is the skyrmion displacement over one period T . It is instructive to change the integration variable in Eq. (25) from time t' to $\Theta' = \Theta(t')$ giving the net skyrmion spatial displacement along the steady-state cycle

$$\Delta x_s \propto \left(\int_{\Theta_A}^{\Theta_B} d\Theta' \xi_{on}(\Theta^{-1}(\Theta')) - \int_{\Theta_A}^{\Theta_B} d\Theta' \xi_{off}(\Theta^{-1}(\Theta')) \right), \tag{26}$$

where the first integral is taken over the on branch (the full blue curve in Fig. 8) of the cycle, and the second integral over the off branch (the dashed orange curve in Fig. 8) of the cycle. Θ_A and Θ_B correspond to the limiting values of Θ at times when the field undergoes jumps from 0 to E and then back to 0, respectively.

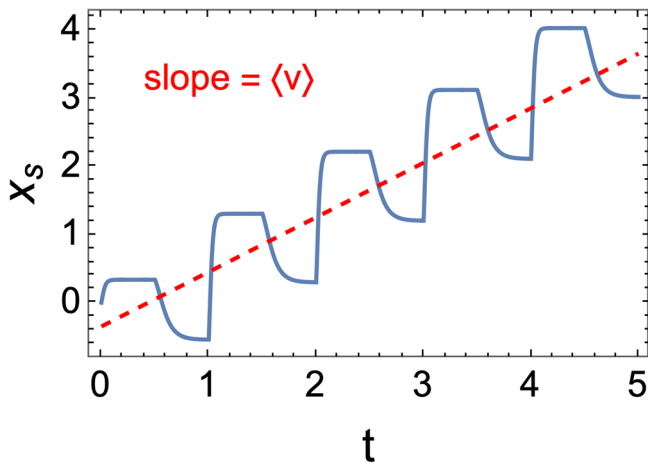


Fig. 9 Skyrmion displacement upon periodic turning of the field on and off. Skyrmion trajectory $x_s(t)$ corresponding to the situation depicted in Fig. 8. Over durations significantly longer than the electric field period, the motion is characterized by a steady average skyrmion velocity $\langle v \rangle$, and the magnitude of this velocity is portrayed by the slope of the dashed red line. The field parameters are $m_{on} = 7, E/W = 1.5, T = 1$ and $\mathcal{D} = 0.5$.

According to (26) Δx_s is proportional to the area enclosed by the steady cycle loop, which is divided into the on branch (the full blue curve in Fig. 8), where the skyrmion moves in the $+\hat{x}$ direction, and the off (the dashed orange curve in Fig. 8) branch, where it moves in the $-\hat{x}$ direction.

The skyrmion trajectory $x_s(t)$ corresponding to Fig. 8 is shown in Fig. 9. The instantaneous velocity is proportional to the rate of change of Θ , and in the linear regime (close to the fixed points) $\Theta \propto \exp(-m^2 t)$. The relaxation of Θ along the field off branch is $1 + (E/W)^2$ times slower compared to the relaxation along the field on branch, such that the larger E/W is, the faster the director rotates away from the axisymmetric configuration favored by the effective anchoring W . This behavior gives rise to an asymmetry between the increasing (field on) and the decreasing (field off) parts of $x_s(t)$, which is clearly visible in Fig. 9.

Next, we compute $\langle v \rangle$ as the average slope of the numerical steady cycle trajectories $x_s(t)$. For the case shown in Fig. 9, $\langle v \rangle$ equals the slope of the red dashed line. $\langle v \rangle$ as a function of the frequency $f = 1/T$ of the pulsed electric field $E(t)$, at selected values of the duty cycle and of field amplitude, is shown in Fig. 10. $\langle v \rangle$ exhibits a maximum at a frequency f_{max} and is always positive. We have varied values of the model parameters in wide ranges and have not observed velocity reversal. As we argue below, this behavior is specific to protocol 1), and velocity reversal may be achieved by introducing a pulsed z -component of the electric field $E_z(t)$, such that $(W + E_z(t))^2 + E(t)^2$ remains constant.

To better understand the emergence of the maximum in $\langle v \rangle$ we examine how steady-state cycles are affected by changing the frequency, which is shown in Fig. 11. Θ increases when the field is turned on, and decreases when it is turned off. Decreasing the frequency from f_{max} allows Θ to relax completely. As a result, the steady-state cycle shown in Fig. 11a, remains unchanged by reducing the frequency even further. The system spends most of the time at the endpoints of the branches. Unchanging steady-state cycles lead to net displacements (over one period) independent of f , such that $\langle v \rangle \propto f$ in the low-frequency regime of Fig. 10.

The reduction in $\langle v \rangle$ at high frequencies is due to the decrease in the range $\Delta\Theta$ of the variation of the background director tilting, and the reduction of the difference between ξ_{on} (the full

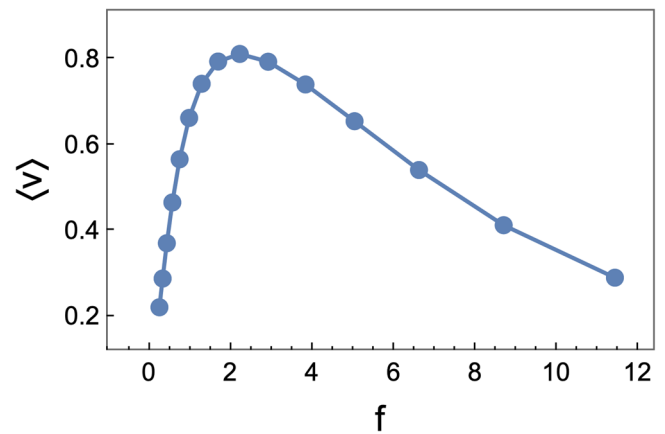


Fig. 10 Skyrmion average velocity. Steady average velocity $\langle v \rangle$ of the skyrmion calculated numerically as a function of the frequency $f = 1/T$. $m_{on} = \sqrt{E^2 + W^2} = 10, E/W = 1.5$ and $\mathcal{D} = 0.5$. The line is to guide the eyes.

blue curves in Fig. 11b) and ξ_{off} (the dashed orange curves in Fig. 11b) in the two branches of the steady-state cycle. We can write the average skyrmion velocity in the following way

$$\langle v \rangle \propto f \Delta\Theta (\overline{\xi_{on}} - \overline{\xi_{off}}), \quad (27)$$

where we used Eq. (26) and introduced an average over Θ width $\overline{\xi_{on}}$ ($\overline{\xi_{off}}$) when the field is on (off). On the other hand $\Delta\Theta < \dot{\Theta}_{max}/f$, and the maximal angular velocity $\dot{\Theta}_{max}$ depends only on the field strength, and not on f , so increasing the frequency will decrease the angular displacement $\Delta\Theta$. This renders $\langle v \rangle < \dot{\Theta}_{max} (\overline{\xi_{on}} - \overline{\xi_{off}})$ which tends to zero as f increases due to the decrease of the difference in brackets.

Figure 12 summarizes the effects of the field strength, the frequency, and the duty cycle upon the skyrmion's average velocity. The velocity is positive in the studied region of the parameter space. This result is directly related to the relaxation behavior of $\xi(t)$, shown in Fig. 6, which in this regime of parameters is effectively monotonically decreasing/increasing along the on/off states. Consequently, the difference $(\overline{\xi_{on}} - \overline{\xi_{off}}) > 0$ for all steady cycles, and the skyrmion velocity is positive. This analysis suggests that for the velocity reversal, there must exist an extended range of times where $\xi(t)$ exhibits a markedly non-monotonic behavior, and where the variation $\Delta\Theta$ of the polar angle is significant. In fact, we observe a weak non-monotonicity in $\xi_{on}(t)$ (the full blue curve in Fig. 6) at early times, which in principle may give rise to velocity reversal. However, the corresponding range of the model parameters around that bump on $\xi_{on}(t)$ is such that the calculated skyrmion speeds are $\sim 10^{-5}$ and our numerical method is not capable of resolving eventual changes in the direction of motion.

Below we show that it is possible to resolve this issue by resorting to another driving protocol. Indeed, in experiments in refs. 12,13, the background angle Θ relaxes faster towards zero when the field is turned off. This is incompatible with driving protocol 1), which renders $\tau_{off}/\tau_{on} = 1 + (E/W)^2 > 1$.

Pulse width modulated electric fields: driving protocol 2). We proceed to consider a driving protocol where $\tau_{on} = \tau_{off}$, which, as it turns out, is sufficient to obtain velocity reversal. To this end, we introduce an additional electric field component in the \hat{z} direction $E_z(t)$, which is in antiphase with the field component in the \hat{y} direction $E(t)$, such that $m = \sqrt{E(t)^2 + (W + E_z(t))^2} = const$. More specifically, in the

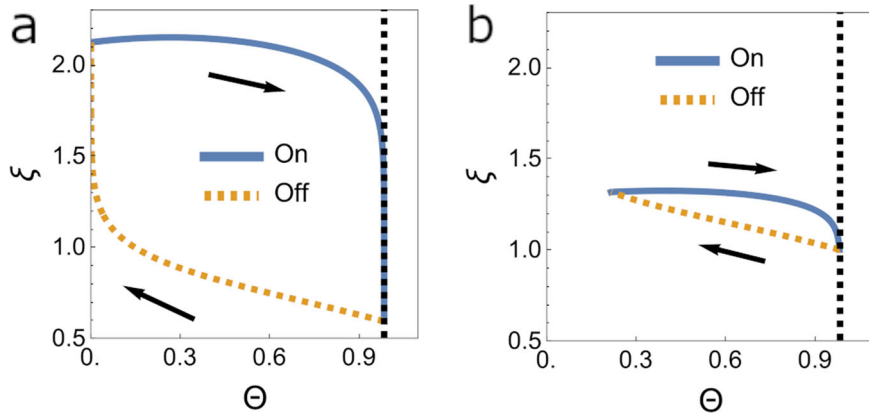


Fig. 11 Steady-state cycle shrinks as the frequency increases. Steady-state cycles of the system in the (Θ, ξ) configuration space. The dashed vertical lines mark the stable Θ when the field is turned on. The values of the parameters are $m_{on} = \sqrt{E^2 + W^2} = 10$, $E/W = 1.5$, $\mathcal{D} = 0.5$, **a** $f = 1$, and **b** $f = 8$. Low frequency in **a** allows the system to cover the full angular range and enables a large difference in ξ when the electric field is on and off, as compared to the high-frequency loop in **b**.

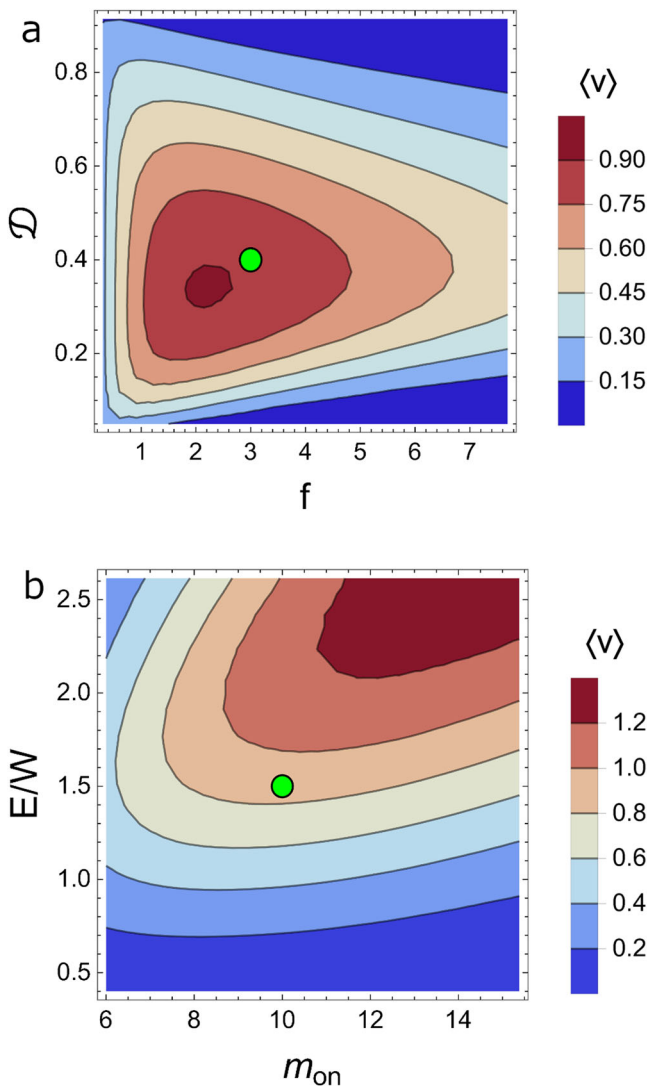


Fig. 12 Heat map of the skyrmion average velocity for driving protocol 1). Color-coded steady average velocity $\langle v \rangle$ of skyrmions moving under pulse width modulated electric fields. **a** $\langle v \rangle$ as a function of \mathcal{D} and f at $m_{on} = \sqrt{E^2 + W^2} = 10$ and $E/W = 1.5$ corresponding to the green circle in **b**. **b** $\langle v \rangle$ as a function of m and E/W at $f = 3$ and $\mathcal{D} = 0.4$ corresponding to the green circle in **a**.

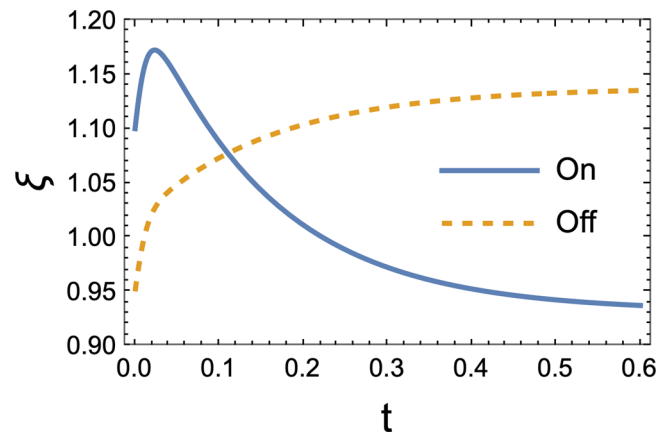


Fig. 13 Relaxation dynamics of the twist wall thickness for driving protocol 2). Thickness ξ as a function of time when the electric field $(0, -E, 0)$ is turned on at $t = 0$, solid blue curve. After ξ relaxes completely, the electric field is turned off, and the corresponding $\xi(t)$ is shown by the dashed orange curve, where $t = 0$ coincides with the time of turning the field off. For both curves $m = \sqrt{E(t)^2 + (W + E_z(t))^2} = 7$. Time is given in units of $\gamma p^2 K^{-1}$.

field off state $E = 0$ and $E_z > 0$, while in the field on state, we set $E > 0$ and $E_z = 0$ to guarantee $m = const$.

An example of the dynamics of ξ under this protocol 2) is shown in Fig. 13. The first difference, when compared to protocol 1) discussed in Fig. 6, is the reduced difference between $\xi_{on}(t)$ (the full blue curve) and $\xi_{off}(t)$ (the dashed orange curve), which will lead to an overall reduction of the skyrmion speed. Secondly, and more importantly, the $\xi_{on}(t)$ has a significant and extended regime of non-monotonic behavior at early times, which enables to tuning of the model parameters, such that $(\overline{\xi_{on}} - \overline{\xi_{off}})$ changes sign. In Fig. 14a, which corresponds to low frequencies, the steady-state cycle explores the whole range of Θ and the loop passes through both fixed points. At the same time, ξ is larger when the field is on, and the skyrmion moves in $+\hat{x}$ direction. At higher frequency, in Fig. 14b, the steady-state cycle shrinks and is attached to the field off fixed point $\Theta^* = 0$, in contrast to Fig. 11b where the dynamics are controlled by the field on fixed point $\Theta^* = \arctan(E/W)$.

Figure 13 shows that when the electric field $(0, -E, 0)$ is turned on, ξ passes through a broad maximum before relaxing to its

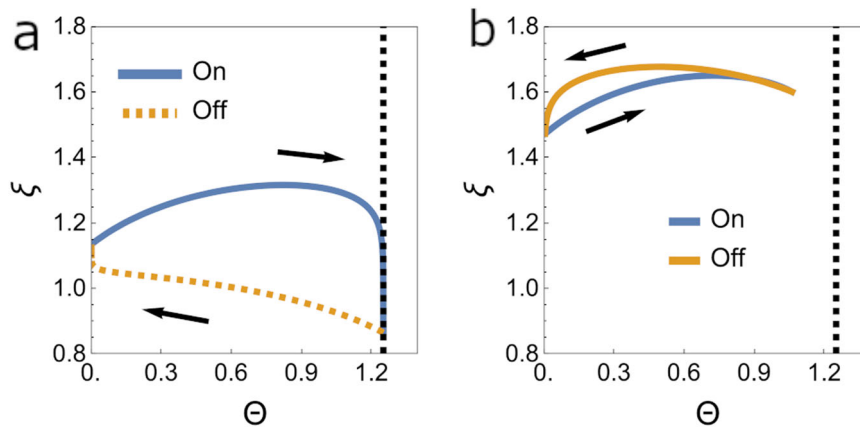


Fig. 14 Steady-state cycles for driving protocol 2). Steady-state cycles of the system in the (Θ, ξ) configuration space for protocol 2), where a vertical component of the electric field $E_z(t)$, oscillating in antiphase with $E(t)$, is introduced such that $m = \sqrt{E(t)^2 + (W + E_z(t))^2} = 7$ for both field-on and field-off states. The dashed vertical lines mark the stable Θ when the field is on. The values of the other parameters are $\arctan(E/W) = 1.25$, $\mathcal{D} = 0.3$, **a** $f = 1$, and **b** $f = 7$. Low frequency in **a** allows the system to fully cover the angular range $\Theta \in [0, \arctan(E/W)]$. In this case, $(\bar{\xi}_{\text{on}} - \bar{\xi}_{\text{off}}) > 0$ leading to a positive skyrmion velocity. High frequency in **b** reduces the angular range covered by the system, and $(\bar{\xi}_{\text{on}} - \bar{\xi}_{\text{off}}) < 0$, which results in a negative skyrmion velocity.

stable value. If the frequency is large enough and the duty cycle is small enough, the $\xi_{\text{on}}(t)$ branch follows the short time increasing part of the on curve in Fig. 13. This behavior is depicted in Fig. 14b by the full blue curve. Next, after the field is turned off the system follows the dashed orange curve in Fig. 14b. Surprisingly, just after setting the field to zero, we observe a growing $\xi_{\text{off}}(t)$, which leads to $(\bar{\xi}_{\text{on}} - \bar{\xi}_{\text{off}}) < 0$ and the velocity reversal.

The color-coded velocity profiles in the (f, \mathcal{D}) and $(m, \arctan E/W)$ planes are shown in Fig. 15a and b, respectively. Figure 15a shows that the most efficient way to reverse the skyrmion velocity is by using the duty cycle. Indeed, by analyzing Fig. 15 we find that the velocity can be reversed by changing \mathcal{D} for any f . By contrast, reversing the velocity by changing f or E can only be achieved in narrow ranges of \mathcal{D} or m .

Discussion

We developed a 2D collective variable model of the driven motion of LC skyrmions. The starting point was a five-parametric axisymmetric *Ansatz* for the director field of a skyrmion with the skyrmion number equal to one. The five parameters are the polar and azimuthal angles of the far-field director; the width of the twist wall around the skyrmion core, and the location of the skyrmion center. Assuming the driving electric field varies in a plane perpendicular to the skyrmion plane, the azimuthal angle can be ignored, as it quickly relaxes to the plane of the electric field, while the skyrmion motion proceeds in the direction normal to that plane. Therefore, only three parameters (collective variables) are relevant for the skyrmion dynamics.

The linear stability analysis of the governing dynamical equations demonstrates that the far-field director relaxes with the characteristic time m^{-2} , where $m = m_{\text{on}} \equiv \sqrt{E^2 + W^2}$ or $m = m_{\text{off}} \equiv W$ for the field-on or field-off states, respectively. Therefore, for this driving protocol the far-field background relaxes slower towards the fixed point \hat{z} , corresponding to zero field. The skyrmion velocity is given by the product of the rate of change of the polar angle Θ and the fixed point value of the twist wall thickness ξ^* (different for field-on and field-off). The resulting displacement of the skyrmion over one period of the pulse width modulated electric field is given, for large periods, by $\Delta x_s = \pi(\xi^*(m_{\text{on}}, E) - \xi^*(m_{\text{off}}, E))/2 < 0$, which follows from the results in Fig. 3.

The full nonlinear model predicts $\Delta x_s \propto \Delta\Theta(\bar{\xi}_{\text{on}} - \bar{\xi}_{\text{off}})$, where $\Delta\Theta$ is the (absolute) range covered by the polar angle Θ over one period, and the symbols with the bars denote $\xi(t)$ averaged over Θ for the field-on and field-off states. We found that Δx_s is always positive for driving protocol 1), i.e., the steady average velocity does not change direction and exhibits a single maximum at certain values of the field frequency, duty cycle, and effective field strength.

Velocity reversal is observed for driving protocol 2) where $m = \text{const}$ independent of the direction of the effective electric field. This renders the relaxation times for the far-field director equal in the on and off states of the cycle. We obtained positive velocity at low frequencies and large duty cycles when the electric field is on most of the time, and negative velocity at high frequencies and small duty cycles when the electric field is off most of the time.

Here, we focused on LCs with positive dielectric anisotropy, and one possible future direction is to study systems with negative ones, which is the case for most experimental systems. Another possibility is to investigate the effects of varying the skyrmion core radius, which was kept constant equal to half of the cholesteric pitch. Additionally, the generalization of the presented approach to many skyrmion systems could shed light on the out-of-equilibrium collective behavior of skyrmions.

Finally, we comment briefly on the relation of the present work to another study carried out recently in the same group³⁶. While in the present work, we considered a minimal model for the dynamics of a single skyrmion director field, represented by a small number of collective variables (using the *Ansatz* to describe the skyrmion texture), in ref. ³⁶ the authors have replaced the skyrmionic textures with Brownian particles subject to time-dependent forces, which represent the skyrmion's tendency to move forwards and backward as the electric field is turned on and off.

Methods

Functions $d_1(\xi)$ up to $d_4(\xi)$ are obtained by the following procedure. First, we construct $t_{ij}(\xi) = \int \mathbf{T}_{ij}(\xi, \mathbf{r}) d^2r$ by carrying out a double integral numerically for a range of values of ξ . Next, the numerical data $t_{ij}(\xi)$ is fitted to simple functions of ξ . We find that functions of the form $a + b\xi^n$, where a, b are fitting parameters, and $n = -2, -1, 0, 1$ are good fits in all cases. The explicit

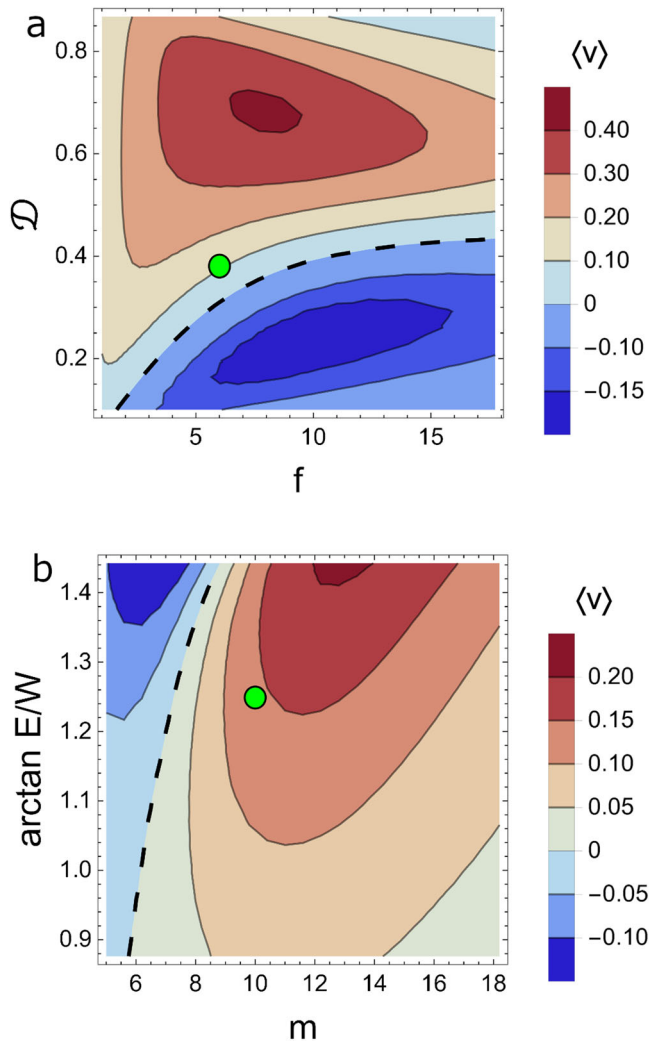


Fig. 15 Heat map of the skyrmion average velocity for driving protocol 2). Color-coded steady average velocity $\langle v \rangle$ of skyrmions moving under an electric field $(0, -E(t), W + E_z(t))^T$, where the time-dependent components asynchronously pulse with the frequency f and the duty cycle \mathcal{D} . **a** $\langle v \rangle$ as a function of \mathcal{D} and f at $m = 10$ and $\arctan(E/W) = 1.25$, corresponding to the green circle in **b**. **b** $\langle v \rangle$ as a function of m and $\arctan(E/W)$ at $f = 6$ and $\mathcal{D} = 0.4$, corresponding to the green circle in **a**. The dashed black lines correspond to $\langle v \rangle = 0$.

expressions for $d_1(\xi)$ up to $d_4(\xi)$ read:

$$d_1(\xi) \approx \frac{\xi}{16.1\xi + 6.5} \quad (28)$$

$$d_2(\xi) \approx 4\pi \left(\frac{0.2}{\xi} - 6.6 \right) \quad (29)$$

$$d_3(\xi) \approx 4(0.5 + 1.9\xi) \quad (30)$$

$$d_4(\xi) \approx \frac{4.9 + 8.5\xi}{15.5 + 9.7/\xi} \approx 0.6\xi \quad (31)$$

Equation (17) for the background polar angle Θ admits an analytical solution

$$\Theta(t) = \arctan \left[\left(E^2 - W^2 + (E^2 + W^2) \tanh \left[\frac{1}{2} t (E^2 + W^2) + \operatorname{arctanh} \left(\frac{-E^2 + W^2 + 2EW \tan(\Theta_0)}{E^2 + W^2} \right) \right] \right) / 2EW \right]. \quad (32)$$

where Θ_0 is the initial (at $t = 0$) polar angle of the background director field. We also provide a special case of the above equation corresponding to the case of zero electric field

$$\Theta(t) = \arccos \left[(1 + e^{-2W^2 t} \tan^2 \Theta_0)^{-\frac{1}{2}} \right]. \quad (33)$$

Data availability

The data that support the findings of this study are available from the corresponding author upon reasonable request

Code availability

The computer codes used to produce the results presented in the article are available from the corresponding author upon reasonable request.

Received: 25 April 2023; Accepted: 29 November 2023;

Published online: 02 January 2024

References

- Manton, N. and Sutcliffe, P. *Topological Solitons* (Cambridge University Press, Cambridge, England, 2004).
- Manton, N. S., Oleś, K., Romańczukiewicz, T. & Wereszczyński, A. Collective coordinate model of kink-antikink collisions in ϕ^4 theory. *Phys. Rev. Lett.* **127**, 071601 (2021).
- Skyrme, T. A unified field theory of mesons and baryons. *Nucl. Phys.* **31**, 556 (1962).
- Mühlbauer, S. et al. Skyrmion lattice in a chiral magnet. *Science* **323**, 915 (2009).
- Yu, X. Z. et al. Real-space observation of a two-dimensional skyrmion crystal. *Nature* **465**, 901 (2010).
- Zhang, X., Zhou, Y. & Ezawa, M. Antiferromagnetic skyrmion: Stability, creation and manipulation. *Sci. Rep.* **6**, 24795 (2016).
- Liu, Y., Lake, R. K. & Zang, J. Binding a hopfion in a chiral magnet nanodisk. *Phys. Rev. B* **98**, 174437 (2018).
- Sutcliffe, P. Hopfions in chiral magnets. *J. Phys. A: Math. Theor.* **51**, 375401 (2018).
- Das, S. et al. Observation of room-temperature polar skyrmions. *Nature* **568**, 368 (2019).
- Smalyukh, I. I., Lansac, Y., Clark, N. A. & Trivedi, R. P. Three-dimensional structure and multistable optical switching of triple-twisted particle-like excitations in anisotropic fluids. *Nat. Mater.* **9**, 139 (2010).
- Ackerman, P. J., Trivedi, R. P., Senyuk, B., van de Lagemaat, J. & Smalyukh, I. I. Two-dimensional skyrmions and other solitonic structures in confinement-frustrated chiral nematics. *Phys. Rev. E* **90**, 012505 (2014).
- Ackerman, P. J., Boyle, T. & Smalyukh, I. I. Squirming motion of baby skyrmions in nematic fluids. *Nat. Commun.* **8**, 673 (2017).
- Sohn, H. R. et al. Dynamics of topological solitons, knotted streamlines, and transport of cargo in liquid crystals. *Phys. Rev. E* **97**, 052701 (2018).
- Sohn, H. R. O., Liu, C. D., Wang, Y. & Smalyukh, I. I. Light-controlled skyrmions and torons as reconfigurable particles. *Opt. Express* **27**, 29055 (2019).
- Sohn, H. R., Liu, C. D. & Smalyukh, I. I. Schools of skyrmions with electrically tunable elastic interactions. *Nat. Commun.* **10**, 4744 (2019).
- Song, C. et al. Commensurability between element symmetry and the number of skyrmions governing skyrmion diffusion in confined geometries. *Adv. Funct. Mater.* **31**, 2010739 (2021).
- Bogdanov, A. N., Röäler, U. K. & Shestakov, A. A. Skyrmions in nematic liquid crystals. *Phys. Rev. E* **67**, 016602 (2003).

18. Duzgun, A., Selinger, J. V. & Saxena, A. Comparing skyrmions and merons in chiral liquid crystals and magnets. *Phys. Rev. E* **97**, 062706 (2018).
19. Duzgun, A., Saxena, A. & Selinger, J. V. Alignment-induced reconfigurable walls for patterning and assembly of liquid crystal skyrmions. *Phys. Rev. Res.* **3**, 012005 (2021).
20. Duzgun, A., Nisoli, C., Reichhardt, C. J. O. & Reichhardt, C. Directed motion of liquid crystal skyrmions with oscillating fields. *N. J. Phys.* **24**, 033033 (2022).
21. Coelho, R. C., Tasinkevych, M. & Gama, M. M. T. D. Dynamics of flowing 2d skyrmions. *J. Phys. Condens. Matter* **34**, 034001 (2022).
22. Long, C. & Selinger, J. V. Coarse-grained theory for motion of solitons and skyrmions in liquid crystals. *Soft Matter* **17**, 10437 (2021).
23. Yu, X. Z. et al. Skyrmion flow near room temperature in an ultralow current density. *Nat. Commun.* **3**, 988 (2012).
24. Krause, S. & Wiesendanger, R. Skyrmionics gets hot. *Nat. Mater.* **15**, 493 (2016).
25. Shen, Y. & Dierking, I. Dynamic dissipative solitons in nematics with positive anisotropies. *Soft Matter* **16**, 5325 (2020).
26. Wu, J.-S. & Smalyukh, I. I. Hopfions, heliknotons, skyrmions, torons and both abelian and nonabelian vortices in chiral liquid crystals. *Liq. Cryst. Rev.* **10**, 34–68 (2022).
27. Samols, T. M. Vortex scattering. *Commun. Math. Phys.* **145**, 149 (1992).
28. Schütte, C., Iwasaki, J., Rosch, A. & Nagaosa, N. Inertia, diffusion, and dynamics of a driven skyrmion. *Phys. Rev. B* **90**, 174434 (2014).
29. Jung, D.-H. et al. Magnetic skyrmion diode: unidirectional skyrmion motion via symmetry breaking of potential energy barriers. *Phys. Rev. B* **104**, L060408 (2021).
30. Miyazaki, Y., Yokouchi, T. & Shiomi, Y. Trapping and manipulating skyrmions in two-dimensional films by surface acoustic waves. *Sci. Rep.* **13**, 1922 (2023).
31. Thiele, A. A. Steady-state motion of magnetic domains. *Phys. Rev. Lett.* **30**, 230 (1973).
32. Gilbert, T. A phenomenological theory of damping in ferromagnetic materials. *IEEE Trans. Magn.* **40**, 3443 (2004).
33. Li, X. et al. Bimeron clusters in chiral antiferromagnets. *npj Comput. Mater.* **6**, 169 (2020).
34. Belongie, S. *Rodrigues' Rotation Formula*. <https://mathworld.wolfram.com/RodriguesRotationFormula.html>. last visited on 14/12/2022 (2022).
35. Tai, J.-S. B. & Smalyukh, I. I. Surface anchoring as a control parameter for stabilizing torons, skyrmions, twisted walls, fingers, and their hybrids in chiral nematics. *Phys. Rev. E* **101**, 042702 (2020).
36. Teixeira, A. S., Tasinkevych, M., & Dias, C. S. Particle-based model of active skyrmions <https://doi.org/10.48550/arXiv.2305.03670> (2023).

Acknowledgements

We acknowledge financial support from the Portuguese Foundation for Science and Technology (FCT) under the contracts: PTDC/FISMAC/5689/2020, EXPL/FIS-MAC/0406/2021, UIDB/00618/2020 and UIDP/00618/2020.

Author contributions

M.T.G. and M.T. conceived the idea. T.A. carried out analytical and numerical calculations. T.A. and M.T. wrote the manuscript. M.T.G. provided critical comments.

Competing interests

The authors declare no competing interests.

Additional information

Supplementary information The online version contains supplementary material available at <https://doi.org/10.1038/s42005-023-01486-5>.

Correspondence and requests for materials should be addressed to Mykola Tasinkevych.

Peer review information *Communications Physics* thanks the anonymous reviewers for their contribution to the peer review of this work. A peer review file is available.

Reprints and permission information is available at <http://www.nature.com/reprints>

Publisher's note Springer Nature remains neutral with regard to jurisdictional claims in published maps and institutional affiliations.



Open Access This article is licensed under a Creative Commons Attribution 4.0 International License, which permits use, sharing, adaptation, distribution and reproduction in any medium or format, as long as you give appropriate credit to the original author(s) and the source, provide a link to the Creative Commons licence, and indicate if changes were made. The images or other third party material in this article are included in the article's Creative Commons licence, unless indicated otherwise in a credit line to the material. If material is not included in the article's Creative Commons licence and your intended use is not permitted by statutory regulation or exceeds the permitted use, you will need to obtain permission directly from the copyright holder. To view a copy of this licence, visit <http://creativecommons.org/licenses/by/4.0/>.

© The Author(s) 2024